Journal of Advanced Joining Processes 10 (2024) 100226

Contents lists available at ScienceDirect

Journal of Advanced Joining Processes

journal homepage: www.sciencedirect.com/journal/journal-of-advanced-joining-processes

Assessment of fatigue crack growth resistance of newly developed LTT alloy composition for the repair of high strength steel structures

Victor Igwemezie [a,b,*], Ali Mehmanparast [c], Supriyo Ganguly [a]

[a] Welding and Additive Manufacturing Centre, Department of Manufacturing and Materials, Cranfield University, UK
[b] Department of Materials & Metallurgical Engineering, Federal University of Technology, Owerri, Nigeria
[c] Department of Naval Architecture, Ocean and Marine Engineering, University of Strathclyde, UK

ARTICLE INFO

Keywords:
Steel
Welding
Residual stress
LTT alloy
Microstructure
Martensite
Fatigue crack growth

ABSTRACT

Tensile residual stress (TRS) is a well-known factor that deteriorate the integrity of welded joints. Fatigue failure is accelerated by the existence of TRS introduced during the welding process. There have been efforts in the last two decades to develop filler alloys that can reduce TRS by introducing compressive residual stress (CRS) to oppose the TRS in high strength steel welded joints. These works are based on the theory of austenite (γ) to martensite (α') transformation and the filler is often called a low transformation-temperature (LTT) alloy. Many studies have reported that the fatigue strength (FS) of weld joint made with LTT alloy is many times better than that of the conventional fillers. It is reported to be particularly useful in the repair of high strength steel structures. However, studies on the fatigue crack growth (FCG) behaviour of these LTT alloys is scarce. In this work, we developed Fe-CrNiMo based LTT weld metal composition, assessed its FCG behaviour and compared the results with that of a conventional welding wire (ER70S-6). It is found that ER70S-6 weld metal obtained under relatively fast cooling is extremely tough, but the associated heat affected zone (HAZ) has poor resistance to FCG which obscured the benefit of the tough weld metal. High heat input or condition that results to slow cooling of the ER70S-6 weldment deteriorates its resistance to FCG. Unfortunately, despite its low martensite start temperature of 231±7 and the anticipated beneficial effect of induced CRS, the LTT alloy studied had the lowest FCG resistance. The LTT alloy appears to have an intrinsic microstructural feature or a 'fault line' that reduced its resistance to FCG. While the LTT alloy weld metal has poor resistance to FCG, the associated HAZ resisted FCG more than the HAZ associated with ER70S-6 weld metal. It is observed that aligning the ER70S-6 weld metal perpendicular to the crack front produced the highest resistance to fatigue crack initiation and propagation. In the case of ER70S-6, it is believed that the weld metal induced a CRS at the notch tip which resulted to the high fatigue resistance. In the case of the LTT alloy, perpendicular alignment of the weld metal produced slight improvement.

Introduction

Localised heating and inhomogeneous cooling of a weld metal (WM) results in the development of tensile residual stress (TRS) in welded structures. Under service loading, the TRS combines with the applied stress to increase the mean stress acting on the structure and this accelerates failure (Masubuchi, 1980; Withers and Bhadeshia, 2001; Fricke, 2005; Ainsworth et al., 2000). There have been efforts in the past years to develop welding alloys to mitigate TRS in welded components – particularly in repaired structures. The design of these alloys is centered on the transformation of austenite (γ) to martensite (α'). In theory, when α' forms from γ in steel, there is a volumetric expansion accompanying the α' transformation (Moyer and Ansell, 1975). Therefore, if a martensitic WM is used as a filler, the weld beads are expected to expand during cooling to the ambient temperature, (Tα). The volumetric expansion is expected to counter the solidification shrinkage forces in the WM as it cools down from elevated temperature and this results to TRS relaxation. To obtain the TRS relaxation benefit, the transform must occur at low temperatures else the TRS state may be worsened (Francis et al., 2007; Bhadeshia et al., 2007). This kind of welding filler is commonly called low transformation temperature (LTT) alloy. The ability of the alloy to redistribute TRS makes it attractive for use in field repairs of high strength steel structures as no heat treatment would be needed – saving time and cost. Thus, the design of LTT alloy is usually centered on reducing the TRS, improving fatigue strength (FS) and

* Corresponding author.
E-mail address: victor.igwemezie@cranfield.ac.uk (V. Igwemezie).

https://doi.org/10.1016/j.jajp.2024.100226

Available online 1 May 2024

Key nomenclature

CRS	compressive residual stress
$Ms._T$	martensite start temperature
LTT	low transformation temperature
WM	weld metal
ER70	ER70S-6
RS	residual stress
PTT	phase transformation temperature
FCG	fatigue crack growth
FCGR	fatigue crack growth rate
FCR	Fatigue crack resistance
T_a	ambient temperature
TRS	tensile residual stress
TS	tensile strength
YS	yield strength
FS	fatigue strength
ce	cellular
de	dendrite or dendritic
ce-de	cellular dendritic
T*i*	interpass temperatures
cc	chemical composition
α_b	bainite
α	allotriomorphic ferrite
α_w	Widmanstätten ferrite
α'	martensite
γ	austenite
γ_r	retained austenite
θ	carbide/pearlite
V_f	volume fraction

reducing distortion associated with the welding - without additional post weld heat treatment.

Many researchers have studied LTT alloys. Ohta et al. (1999, 1999, 2001, 2003) in their study developed a welding alloy named 10Cr-10Ni to improve the fatigue performance of welded joints by reduction of the TRS. The main property of this alloy is that the α' transformation at low temperature resulted to a development of compressive residual stress (CRS) that considerably countered the solidification shrinkage. Ohta et al., in one of their studies (Ohta et al., 2003) compared the fatigue strength (FS) of the 10Cr-10Ni and conventional welding filler (MGS-63B) on a SM570Q baseplate. The FS of the 10Cr-10Ni was reported to be superior with a fatigue limit of about 475 MPa while that of MGS-63B was about 300 MPa. It was also reported that the CRS was induced around the weld toe of the lap joint which led to significantly improved fatigue life. In another study, Ota et al. (2000) compared the FS of box joint welded with 10Cr-10Ni and some other conventional welding alloys on HT580 steel plate. The fatigue limit of the HT580 steel welded with the conventional alloy was reported as 65 MPa while that of 10Cr-10Ni was around 130 MPa. The improvement in the fatigue performance of the 10Cr-10Ni was almost twice that of the conventional alloy. Ota et al. (2001) also studied FS of out-of-plane gusset HT780 specimen welded with 10Cr-10Ni. He reported that the FS was about three times higher than the conventional filler. Generally, this fatigue improvement was attributed to stress ratio effect and the differences in the effective stress range. The TRS peak in the conventional alloy added to the fatigue test load, increasing the stress range, and leading to poor fatigue performance. In yet another study, Ohta et al. (1999) compared the fatigue crack growth rate (FCGR) of joints welded with 10Cr-10Ni and a conventional wire on a SPV490 baseplate. They machined a notch through a butt WM in a rectangular cross-sectional bar specimen. They reported that the LTT alloy decelerated the FCGR significantly in comparison with the conventional alloy. However, the LTT welded sample was heat treated at about 720 °C and cooled in air. Hence, the fatigue crack retardation performance reported does not represent the as-welded condition and should not be attributed entire to the LTT wire transformation.

Eckerlid et al. (2003) assessed the mechanical strength, impact toughness, and fatigue properties of LTT alloy named B206 and conventional fillers - Ok Autrod 12.51 and Filarc PZ6119 using a Domex 700 base plate. They reported that the B206 improved FS of box-welded joint more than the conventional fillers. The improvement appeared to increase with decrease in the value of the applied fatigue stress range. Important points to note in their study is that the LTT alloy reduced the TRS mainly at the weld toe and that the induced CRS shifted the point of crack initiation from the weld toe to the weld root. The study also suggested that the number of beads and the type of fatigue waveform could affect the fatigue result. It also indicated that fatigue peak load could relax the beneficial CRS thereby reducing the effectiveness of the LLT alloy. In other studies (Ooi et al., 2014; Karlsson and Mraz, 2011; Bhatti et al., 2013; Matsuzaki et al., 2020), the FS of the LTT alloy was found to be about 3 times or higher than that of the conventional one.

Hensel et al. (2020) in their study assessed the fatigue resistant of a joint made with the combination of conventional filler with good impact toughness but low FS and Fe-CrNi based LTT filler with high FS, but low toughness. The baseplates were S355J2+N steel and high strength steel S960QL. The LTT filler was used as an additional weld bead to a circumferential conventional bead. They applied the LTT alloy around the areas that were prone to fatigue crack initiation – such as the weld toe at the end of the welded longitudinal stiffeners. They found that the application of LTT in this way improved FS, and the value was higher in the S960QL. Hensel et al. (2020) attributed the increase in FS as compared to S355 steel to the stability of the CRS field and low TRS in the S960QL steel.

Miyata and Suzuki (2015) developed an LTT alloy by increasing the Mn and Ni contents to lower the martensite start temperature ($Ms._T$). Here the conventional use of Cr to lower the $Ms._T$ was eliminated. In their work, they combined conventional and LTT welding alloys and reported that the conventional filler had good toughness (or crack resistance), but low FS due to the TRS at the weld root and toe. The crack resistance in the LTT was reported to be poor, but the FS is improved due to the existence of the CRS. For the combined conventional and LTT joint, the crack resistance was reported to be good, and the FS improved due to the CRS induced by the LTT at the weld toes. In general, many researchers have reported that LTT alloy improved the FS of welded joint many times over the conventional fillers (Ota et al., 2000; Ota et al., 2001; Eckerlid et al., 2003; Ooi et al., 2014; Karlsson and Mraz, 2011; Bhatti et al., 2013; Miyata and Suzuki, 2015).

Miki et al. (2012) assessed the FCGR in a CRS field induced by LTT weld repair of α-pearlite steel of σ_{YS} and σ_{TS} of 439 MPa and 556 MPa respectively. They used a gouged and repaired C(T) specimen in their study. They assessed the FCGR in the LTT WM after repair. From the data presented for the LTT No.2 in Fig. 11, for the unrepaired specimen, the crack initiated or started growing at stress intensity factor range ΔK of about 12 MPa$\sqrt{m}$ with crack growth rate of about 2.94E-06 mm/cycle. For the repaired specimen, the crack initiated or started growing at ΔK of about 45 MPa$\sqrt{m}$ with crack growth rate of about 1.11E-05 mm/cycle. Thus, the start of the fatigue crack growth was delayed to 45 MPa$\sqrt{m}$ in the repaired sample and the Paris region of the repaired sample is steep. This means that the crack growth rate would be higher in the repaired sample. Thus, the CRS from the LTT appears to have improved the crack growth start life, but as soon as the crack started growing the rate was higher than that of the unrepaired specimen.

Despite these successful studies, there are no commercially accepted LTT alloy in the market today. Karlsson et al. (2010) identified 13Cr 6Ni

composition as a promising LTT alloy, but the resistance of the alloy to fatigue crack growth in a repaired scenario – either for single or multiple passes is yet to be seen. There are some unresolved issues associated with LTT alloy (Igwemezie et al., 2022). The alloy, apart from inducing CRS at the weld areas must possess baseline fracture resisting microstructure to avoid sudden failure in the event that the CRS is relaxed by say overloading of the component or by stress redistribution that occurs as crack propagates in a stress field. The alloy must also have good weldability to avoid defects.

The determination of FS is a common method used in assessing the performance of LTT alloys in most studies. Presently, there are few studies (Ohta et al., 1999; Miki et al., 2012) on the FCG behaviour of LTT alloys. Therefore, broad understanding of the FCG behaviour of LTT alloys is important if they are to be useful in repairing thick steel sections that will serve in fatigue environment – this forms the motivation for this study. In this work, we developed Fe-CrNiMo based LTT WM composition. We used this composition to repair grooves in C(T) specimens. To measure the integrity of the repaired region, the FCG resistance of this alloy was evaluated, and the performance was compared with that of conventional ER70S-6 welding wire. This information is needed to assess the advantages of the LTT alloy over the conventional wire in the repair of steel structures.

Materials and method

Development of LTT weld metal composition

ER70S-6 (or ER70) is a conventional filler wire in the welding of structural steels. It comes in the form of uncoated wire that is commonly used in MAG and TIG welding processes. The common composition of the filler wire is given in Table 1. The major elements are C, Mn, and Si. The 1.46 wt.% Mn in the ER70 was within the optimum limit (1.5 wt%) that refines microstructure and improves impact toughness (Evans, 1980). The chemical composition of the ER70 was modified using Fe-CrNiMnMo alloy wire with composition also shown in Table 1. The modification was carried out using Cold Wire GMA (CW-GMA) process. The CW-GMA system is made up of KUKA robot, CMT power source, cold wire feeding system, electrical characteristics monitoring system, and molten metal shielding system. The CMT process was used to ensure low heat input, elimination of spatter and reduction of dilution from the baseplate. Automated CW-GMA was used to ensure that all the mixing parameters were consistent and repeatable.

To establish the CW-GMA parameters, first ER70 wire of 1.2 mm diameter was positioned as the hot wire (HW) and Fe-CrNiMnMo alloy wire of 0.8 mm diameter as the cold wire (CW) as shown in Fig. 1(a). Five factors that affected the CW-GMA were the HW feeding speed, CW feeding speed, CW feeding angle (θ), contact tip to workpiece distance (CTWD) and the arc length correction (AC). These factors were varied independently until good, uniform bead, low heat input and little or no spatter was obtained. Fig. 1(b) shows sample of beads obtained by varying these factors. For example, in Fig. 1(b), the beads 1, 2, 3 and 4 were considered inadequate while bead 5 is adequate. The parameters that gave good and uniform bead for the alloy mixing are given in Table 2. The melt pool was protected using 80 %Ar + 20 %CO_2 shielding gas at pre-flow rate of 18 L/min and mixing flow rate of 15 L/min.

ER70 WM composition was modified by feeding the cold Fe-CrNiMnMo alloy wire into its melt pool. The feeding speed for the ER70 wire was 7.0 m/min. By adding the cold wire at various feeding speeds, LTT WMs with different compositions were produced. During the mixing process, the amount of the alloying solutes increased – resulting in the formation of martensite (α') under normal cooling condition. Hence, each LTT WM composition produced was evaluated for cracking tendency. The intention of the cracking test was to eliminate brittle WM compositions. To do this economically, a simple cracking test was devised. This involved preparing a groove with 90° included angle on steel baseplate. The groove was filled with WM deposited using the parameter listed in Table 2. The set up for the welding is shown in Fig. 2(a). Six passes were used to fill the groove. Fig. 2(b) shows a typical 6-pass welded sample. The groove dimensions and bead sequence for the weld are shown in Fig. 2(c). An interpass temperature (T_i) of about 100° was used.

The 6-pass weldment was allowed to cool down. After cooling to the ambient temperature (T_a), the 7th pass was then placed at the middle of the previous weld beads as shown schematically in Fig. 3(a). The weldment is then allowed to cool again to T_a. Fig. 3(b) is a typical 7 passes weldment and the notch or weld toe in the encircled areas were examined for cracks for the various compositions formed. In this way, obviously brittle compositions were eliminated. Note that the crack that results at the end of the test is due to residual stress level at the weld notch, not because of any external load. Fig. 3 (c & d) show typical cracking observed for some compositions and Fig. 3(e) shows a composition that has no cracking. The compositions with little or no cracking were selected for fatigue crack growth testing.

In Fig. 4(a), the area in the rectangle was used in the determination of the chemical composition of the WMs. This region was chosen because it is expected to have little or negligible dilution from the baseplate. The LTT WM compositions were determined using Optical Emission Spectroscopy (OES) Analysis. In the OES technique, an electrical charge was applied to the sample, vaporizing a small amount of the material. The OES spark discharged a plasma with a distinct chemical mark. This allowed for the determination of the percentage breakdown of the constituent elements in weight percentages.

The transverse sections of the weldment were cut as shown in Fig. 4 (b) for hardness testing. Five hardness values, from position 1 to 5 were taken across each WM as shown by the scheme in Fig. 4(c). Vickers hardness testing was implored using 2 kg load and 3 mm spacing from the top to bottom. Hardness of ER70 WM was also measured and then compared with that of LTT WM. The reported hardness is the average of 3 values in each case for the 5 positions. Also, the microstructure of the transverse surface of the welds were examined.

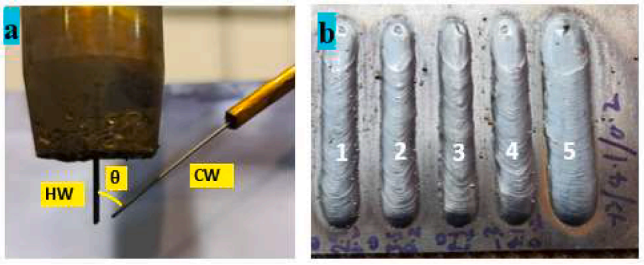

Fig. 1. Alloy mixing procedure: (a) Positioning of the HW & CW, (b) beads on plate.

Table 2
Welding parameters for the CW- GMA alloy mixing.

CTWD	15 mm
ER70 feeding speed	7.0 m/min
CW feeding speed	45–47°
Arc correction	0 %
Shielding gas	80 %Ar + 20 %CO2
gas flow rate	15 L/min
Average voltage	19.48 V
Average current	196 A

Table 1
Typical chemical compositions of ER70S-6 and modifying wires in wt%.

Grade	C	Mn	Si	Cr	Ni	Mo	Cu	Nb
ER70S-6	0.08	1.46	0.85	–	–	–	–	–
Fe-CrNiMnMo	0.01	4.60	0.12	25.0	22.0	2.2	0.02	0.01

Fig. 2. (a) Welding set up: (b) 6-pass welded sample, (c) schematic of the 6-pass bead sequence.

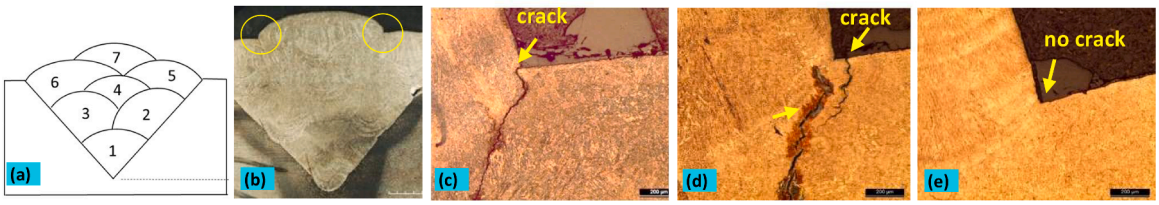

Fig. 3. Weld metals: (a) schematic of 7-pass weld, (b) 7-pass weldment showing toe or notch area examined, (c & d) typical cracking observed in the LTT alloy, (e) LTT alloy composition with no cracking.

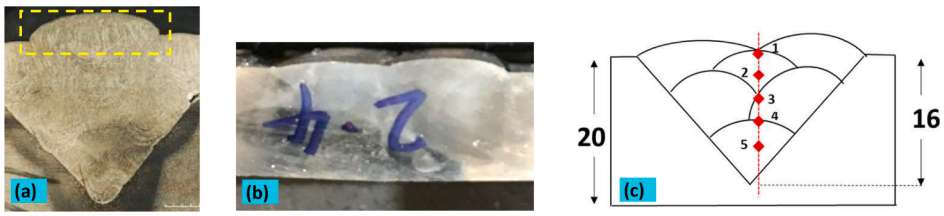

Fig. 4. Composition and hardness measurements: (a) location of compositional measurement (b) cut section for hardness test, (d) hardness measurement scheme.

Table 3
Wire feeding rate for the LTT WMs and ER70.

Samples	Feeding speed (m/min)
LTT1	2.0
LTT2	3.0
LTT3	5.8
ER70a	0.7
ER70b	4.1
ER70c	4.6
ER70 HW = 7.0 m/min	

Determination of the phase transformation temperature (PTT) of the weld metals

The compositions of the LTT WM produced by feeding the cold Fe-CrNiMnMo modifying wire into the ER70 weld pool at the rate of 2.0, 3.0 and 5.8 m/mm respectively were selected. The LTT WMs produced were denoted LTT1, LTT2, LTT3 as shown in Table 3. The Phase transformation temperature (PTT) of the solidifying WM was determined by carefully inserting R-type thermocouple into the weld pool as shown in Fig. 5. The thermocouple was inserted into the second pass of the WM deposition. This is to ensure that the WM composition measured has little or negligible dilution from the baseplate. Three measurements were recorded for each bead and the data generated were collected from the associated computer logging system. To evaluate the sensitivity and consistency of the thermocouple, ER70 CW of 0.8 mm diameter was fed into the ER70 HW of 12 mm wire diameter at 0.7, 4.1 and 4.6 m/min to produce different cooling rates. The WMs were labelled ER70a, ER70b and ER70c as shown in Table 3. The deposition was made using the parameters in Table 2.

The maximum temperature of the WM captured by the thermocouple was 1500 °C and it was then allowed to cool to the ambient temperature

Fig. 5. Use of R-type thermocouple to measure phase transformation temperature.

(T_a). During cooling, phase reaction is expected to occur, and this shows up as a sudden change along the curve due to recalescence. Recalescence is the increase in temperature resulting from change in crystal structure (i.e., phase change). When γ decomposes into other phases, latent heat (or heat of transformation) is released. This heat causes a temporary increase in the temperature of the solidifying metal. This becomes detectable only when the rate of dissipation of the transformation heat is higher than that of the normal heat dissipation while cooling the metal

through the transformation temperature range. The start of the sudden change on the cooling curve was recorded as the PTT. The PTT was also calculated using multiple regression models found in the literature (Overview, 2022; Gramlich et al., 2020). The equations are reported to provide good estimates for steels having carbon content that is less than 1.0 wt%. Comparison of the model predictions with that of the experimentally estimated values was made.

Evaluation of the fatigue crack growth behaviour of ER70 and the LTT alloy weld metals

Test material - baseplates

The baseplates for the FCG resistance tests were 20 mm thick API 5L-X100 and S355J2+N steel grades. The X100 is a high strength steel designed for pipelines. The S355J2+N grades are commonly used for structural applications across many platforms, such as onshore/offshore platforms and wind turbine support structures. Fig. 6 shows the mechanical properties of the steel grades and the associated microstructures. The X100 steel microstructure has fine grain structure without banding. Its microstructure consists of carbides/granular bainites uniformly distributed in the α matrix. This refinement is due to its higher alloying elements and production process. The microstructure of the S355J2+N (or S355) steel grade consists fundamentally of ferrite (α) matrix with banded pearlite (θ), as noted in Fig. 6. Table 4 shows the mechanical properties and chemical compositions in wt% of the steel grades.

The 0.2 % YS and UTS of the X100 are 602 MPa and 760 MPa and that of S355 are 408 MPa and 525 MPa respectively. The% strain at the UTS is 13 for X100 and 23 for the S355, while the% strain at failure is 20 for the X100 and 36 for the S355.

Specimen preparation

Compact tension (C(T)) samples were extracted from the baseplates as shown in Fig. 7. The samples were gouged in 3 different ways as shown in Fig. 7(a–c) with dimensions in accordance with Refs. (ASTM, 2015; BSI, 2008). The gouged samples were used to simulate different scenarios in repair welding. It should be noted that most studies (Moe et al., 2023; Song et al., 2021; Jacob et al., 2019) cut their C(T) samples from already welded stock. This practice redistributes or relaxes the as-deposited residual stress field which would affect the FCG rate results obtained. In this study, the as-welded residual stress field is preserved. The C(T) samples were designed to test the FCG resistance of the WM (Fig. 7(a)), across the WM (Fig. 7(b)), and the HAZ (Fig. 7(c)). The transverse orientation also was used to evaluate the effect of the WM columnar grain orientation and CRS that occurs away from the weld centreline. Also, the orientation of Fig. 7(c) was chosen to assess the influence of the CRS induced by the LTT WM on the FCG resistance of the HAZ. The pictures of physically gouged samples are shown in Fig. 7 (d, e & f), while that of the welded samples in Fig. 7(g–i). The excess WM resulting from the weld deposition on the C(T) sample was ground off before fatigue crack growth testing to make the results comparable (see Fig. 7 (j–l).

One set of the C(T) samples was welded with the LTT compositions, and another set welded with the ER70. A robotic CW-GMA system was used to eliminate the inherent inconsistency in manual welding. Three weld passes were used to fill the gouged area. The welding parameters are shown in Table 5 and other parameters can be found in Table 2. The S355 samples experienced relatively rapid cooling. The heat input is higher for the X100 samples to ensure good weld fusion.

Test set-up and crack length measurement

Instron 8801 Machine was used to perform the FCG test and has been reported in reference (Igwemezie et al., 2018). The tests were in accordance with references (ASTM, 2015; BSI, 2008). The fatigue load of 20 kN, loading ratio of 0.1 and frequency of 5 Hz were used. The tests were conducted at laboratory T_a in the range 17 - 20 °C. The C(T) specimen was accurately aligned perpendicularly to the loading axis using spirit level as shown in Fig. 8(a) and the specimen centralized within grips. Before setting C(T) specimen into the fatigue machine's grips, its surface was polished with 400 grit abrasive paper and using indirect optical fibre lighting to aid in the resolution of the crack tip before crack length measurement. The crack length measurements in air followed the process outlined in reference (Igwemezie et al., 2018). Sinewave of constant amplitude loading, and a constant mean load was employed as shown in Fig. 8(b). Crack length, (a) was measured on the specimen using StreamPix5 digital cameras and in some cases travelling microscope.

To take readings, the waveform was held at 98 % of the 20 kN for 20 s as shown in Fig. 8(c). This interruption of cyclic loading to take readings is permissible (ASTM, 2015) if care is taken to avoid introducing transient crack extension under static force. Fig. 9(a) shows typical positioning and measurement of the crack length using StreamPix5. Firstly, a scale was placed on the sample and the software was then used to capture this scale. The captured scale is then used in subsequent measurement of the crack length, a in a horizontal position. Camera or travelling microscope was used to check differences in a between both sides of the C(T). If at any point the difference between the crack lengths at both sides exceeds 3 mm the test is terminated. Again, if the main crack from the notch is growing and other cracks initiated from various sources the test is terminated or the total number of cycles to failure recorded. Fig. 9 (b) shows the positioning of the notch tip at the HAZ. Here the intention is to determine the crack growth resistance in the HAZ. If HAZ is less resistant, then crack is expected to travel through it, otherwise it will divert and travel through the WM or the parent metal. During the tests, the number of cycles (N) that elapsed and the a were recorded as shown in Fig. 9(c).

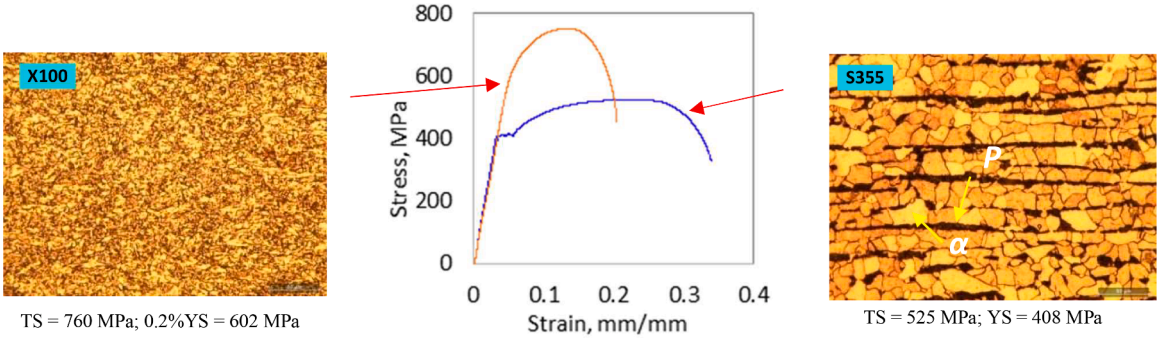

Fig. 6. Microstructure and mechanical properties of the baseplates.

Table 4
Composition of API 5L-X100 and S355 baseplates in wt.%.

(A) Grade	C	Mn	Si	Cr	Ni	Mo	Cu	V	Nb	Ys (Mpa)	Ts (Mpa)	εUTS(%)
S355	0.15	1.47	0.21	0.04	0.05	0.002	0.03	0.001	0.02	408	525	23
X100	0.08	1.81	0.10	0.02	0.46	0.24	0.26	0.001	0.02	602	760	13

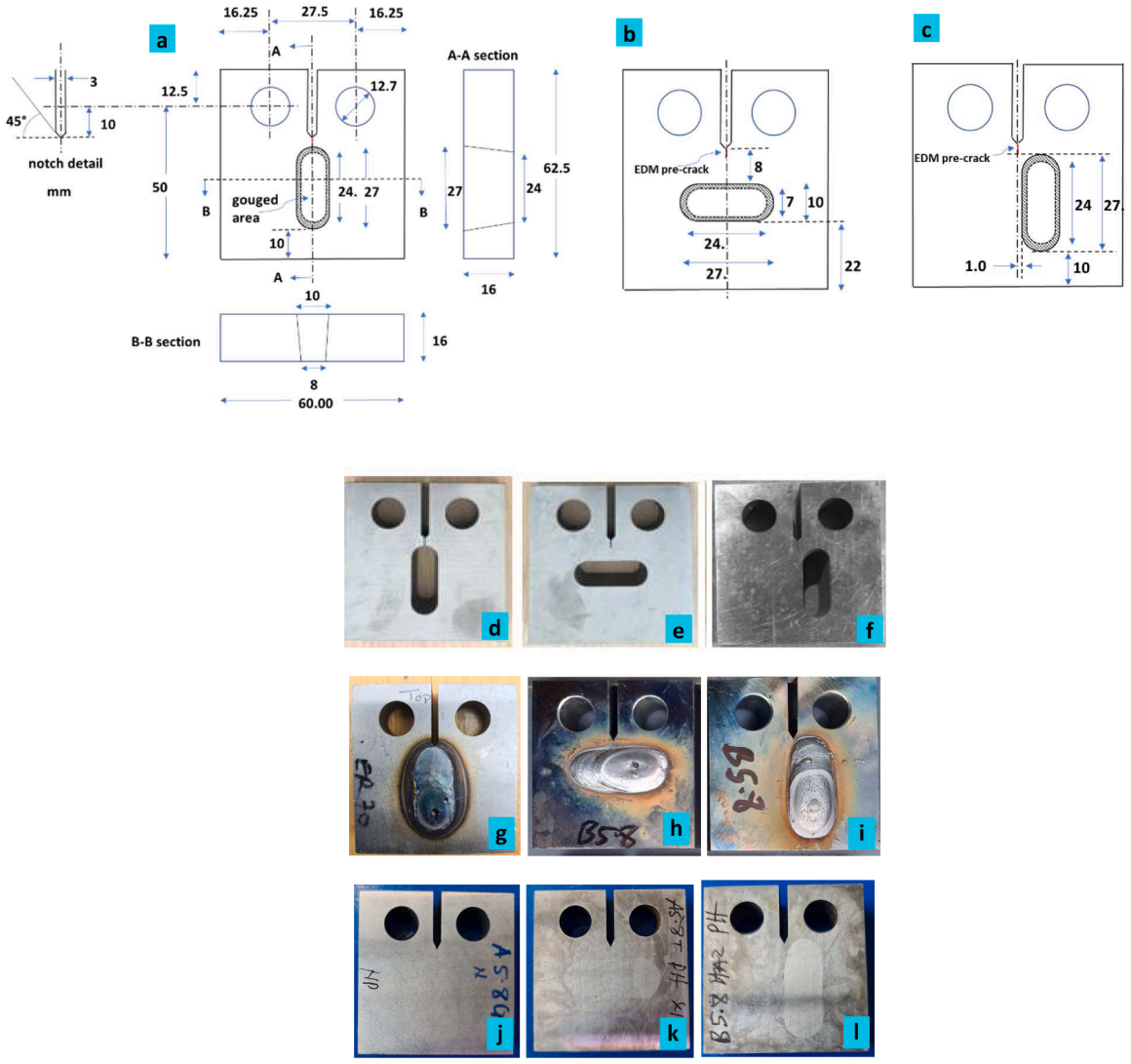

Fig. 7. Gouged standard compact tension experimental samples.

Table 5
Welding parameters for the C(T) samples.

	S355 baseplate	X100 baseplate
Average voltage	19.57 V	21.0 V
Average current	198 A	225 A
Interpass temperature	~100° °C	~ 150 °C

Calculation of fatigue crack propagation rate

The FCG rate calculation was carried out in accordance with linear elastic fracture mechanics (LEFM) and as specified in ASTM E647–15 (ASTM, 2015) and BS EN ISO 11782-2:2008 (BSI, 2008). For the C(T) specimen, the change in stress intensity factor range (ΔK) during cyclic loading was calculated from:

$$\Delta K = \frac{\Delta P}{B\sqrt{W}} * \frac{(2+\alpha)}{(1-\alpha)^{1.5}} * \left(0.886 + 4.64\alpha - 13.32\alpha^2 + 14.72\alpha^3 - 5.6\alpha^4\right), \quad valid\ for\ \frac{a}{W} \geq 0.2.$$

where ΔP is the applied cyclic load range, B is the C(T) specimen thickness (16 mm), W is the width of the specimen (50 mm), a is the crack length ($22.5 + \Delta a$) and $\alpha = a/W$. The a vs. no. of cycles (N) from the fatigue tests is plotted. From the a vs. N data, 7-point incremental polynomial method was used in determining the crack growth rate, da/dN. For the 7-point incremental polynomial, 7 successive data points were used to determine each da/dN value. The local range or subgroup used to calculate each value is illustrated in Fig. 9(c). Alternatively, for a parabolic a vs. N curve, polynomial function can be fitted to the curve and the derivative of this function is then used to determine the da/dN values. The results from both methods were found to be similar. The

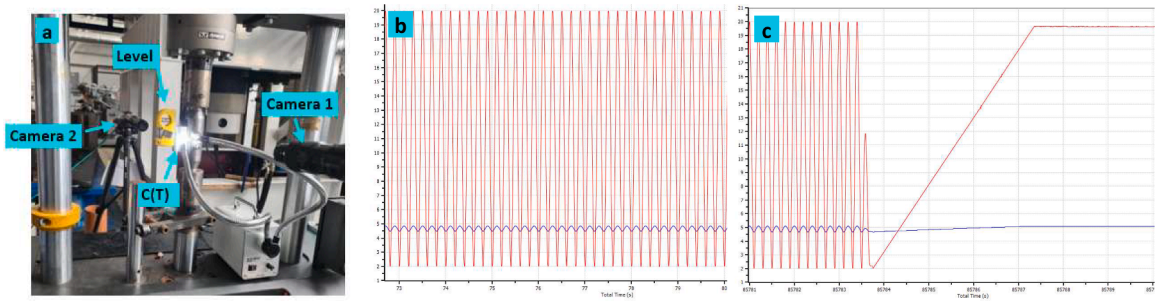

Fig. 8. (a) FCG test set-up, (b) sinusoidal waveform of constant amplitude and 5 Hz for the present study, (c) holding at 98 % of 20 kN for 20 s to measure crack length.

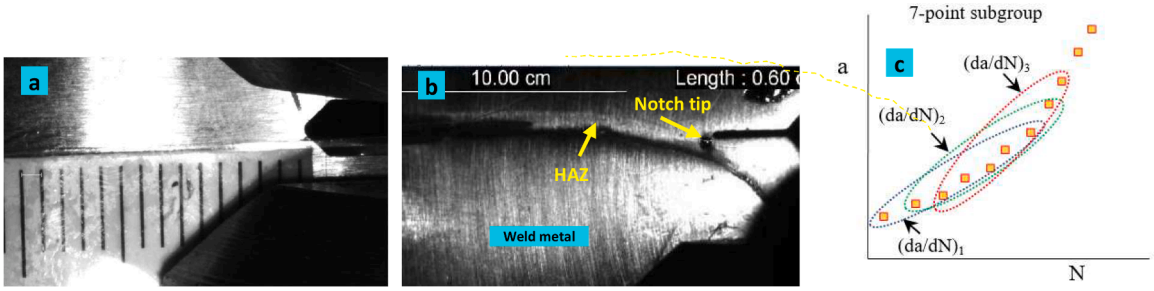

Fig. 9. Optical fibre illumination of C(T) samples: (a) Measurement of crack length (b) positioning of notch tip at the HAZ to measure crack propagation rate, (c) crack length vs. number of fatigue cycles.

value of the *da/dN* was plotted against the corresponding ΔK on a log-log graph. The units m/cycle for *da/dN* and MPa$\sqrt{m}$ for ΔK were used. The Paris law is given as: $da/dN = C(\Delta K)^m$ where C and m are empirical power-law constants found by fitting a regression line to the fatigue test data.

Results and discussion

Chemical composition and cracking test

Table 6 presents the general chemical compositions of the selected LTT 1, LTT 2 and LTT 3 alloys developed in this study - determined using OES Analysis. The shaded area is the composition of interest. Mn, Cr, Ni and Mo form the major alloying elements and their solutes increased from LTT 1 to LTT 3. The variation in the C, Si, Cu, V or Nb down the column is relatively negligible. Also included in the table are the Cr and Ni equivalents of the WM compositions. Fig. 10 shows the notch formed by the 7-pass weld during the cracking test. Small crack was observed at the notch for LTT1 and LTT2 while LTT3 did not show any crack as indicted in Fig. 10(c). It was generally discovered that the LTT WMs with lower alloying solutes were prone to cracking. Kromm (2011) reported that high alloying elements increased the volume fraction (V_f) of retained austenite (γ_r). Thus, the cracking tendency appeared to decrease as the V_f of the γ_r is increased.

Phase transformation temperature (PTT) of the weld metals

To assess the consistency and sensitivity of the R-type thermocouple in measuring the phase transformation start temperature, ER70 CW of 0.8 mm diameter was fed into the ER70 HW of 12 mm wire diameter at 0.7, 4.1 and 4.6 m/min to produce different cooling rates (see Section 2.1). Sudden change along its cooling curve was observed as shown in Fig. 11(a). This was recorded as the point of recalescence or change in crystal structure. The temperature of phase transformation for the ER70 at different cooling rates appears to be consistent. The temperature at which this changed happened was roughly estimated to be in the range 636 ± 2 °C. To confirm the suitability of R-type thermocouple in determining the PTT for the LTT alloy, two beads on plate of LTT2 composition - labelled LTT2a and LTT2b were made and the curve at different cooling rates in air observed. The average temperature at which change in crystal structure occurred was roughly estimated to be in the range of 340 ± 3 °C, as shown in Fig. 12(b). The close values of the PTT were considered to be adequate.

Study has shown that recalescence occurs during transformation of γ to α' (Guo et al., 2017). Thus, this change in the cooling curve is taken to be that due to the transformation of γ to α'. Hence, the start of the change was assumed to be the α' start temperatures denoted here as $Ms._T$. Thus, the $Ms._T$ values of LTT1, LTT2 and LTT3 were determined roughly as 385 ± 7, 340 ± 3 and 231 ± 7 °C respectively and the comparison of the cooling curves is shown in Fig. 11(c). It was observed that as the alloying solutes increased, the kink on the cooling curve became difficult to discern. This was particularly the case for the LTT3. This may be that the rate of dissipation of transformation heat was not high enough to be detected by the thermocouple. This appears to be the case because Kromm et al. (Kromm, 2011) have reported that high alloying elements increased the volume fraction of the γ_r. In summary,

Table 6
Chemical compositions (in wt.%) of LTT weld metal.

LTT series	C	Si	Mn	Cr	Ni	Mo	Cu	V	Nb	Cr_eq	Ni_eq
LTT1	0.09	0.60	1.50	3.55	2.34	0.32	0.018	0.008	0.001	4.77	5.79
LTT2	0.08	0.56	1.74	3.81	3.44	0.48	0.017	0.012	0.003	5.13	6.71
LTT3	0.07	0.47	2.28	6.48	5.40	0.79	0.017	0.022	0.008	7.98	8.64

Cr_eq =%C +%Mo + 1.5 %Si + 0.5Nb; Ni_eq =%Ni + 30 %C + 0.5 %Mn.

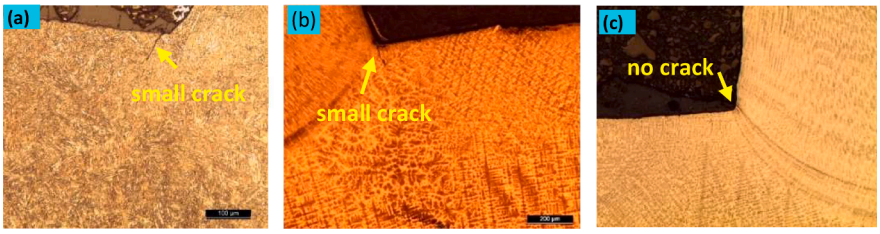

Fig. 10. Results of cracking tests on (a) LTT1, (b) LTT2 and (c) LTT3 weld metals.

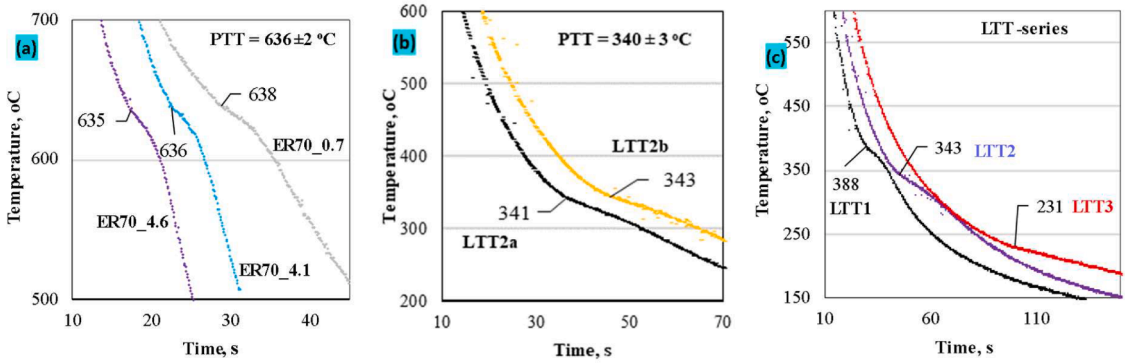

Fig. 11. Cooling curves for rough determination of PTT for: (a) ER70S-6, (b) LTT2 composition, (c) LTT series.

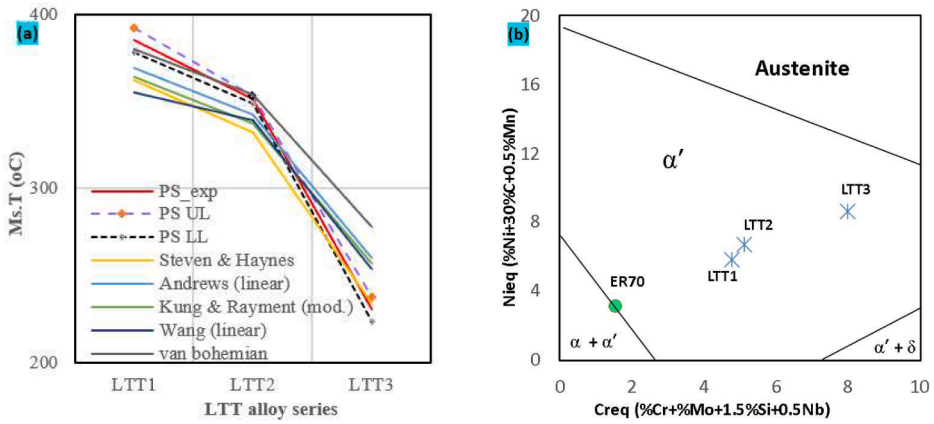

Fig. 12. (a) Comparison of the experimental and calculated $Ms._T$ values, (b) Schaeffler diagram showing the predicted microstructure of the ER70 and LTT series.

Table 7
Multiple regression models used in calculating $Ms._T$ (°C).

Source	Models/ (°C)
Steven & Haynes (Steven and Haynes, 1956)	$Ms._T = 561 - 474C - 33Mn - 17Cr - 17Ni - 21Mo$
Andrews (linear) (Andrews, 1965)	$Ms._T = 539 - 423C - 30.39Mn - 12.14Cr - 17.69Ni - 7.46Mo$
Kung & Rayment (mod.)	$Ms._T = 539 - 423C - 30.4Mn - 12.1Cr - 17.7Ni - 7.5Mo - 7.5Si + 10.0Co$
Wang (linear) (Wang et al., 2000)	$Ms._T = 545 - 470C - 37.7Mn - 3.96Si - 21.5Cr - 38.9Mo$
van bohemian (Van Bohemen, 2012)	$Ms._T = 565 - 600(1 - e^{-0.96C}) - 31Mn - 13Si - 18Ni - 10Cr - 12Mo$

the lowest $Ms._T$ of 231± 7 °C was recorded for LTT3 and the reaction occurred after about 1 min 41 s.

The $Ms._T$ obtained was on small portions of the WM and may not represent the $Ms._T$ condition everywhere in the WM due to chemical inhomogeneity. Hence, the value is expected to fluctuate within a particular narrow range. The $Ms._T$ was then calculated using multiple regression models. A total of 30 regression models were queried (Overview, 2022; Gramlich et al., 2020) and the five regression models that produced close estimates to the experimental values are listed in Table 7. The comparison of their predictions is given in Table 8. The PS is the experimental data of the present study. The PS_{UL} is the upper limit and PS_{LL} the lower limit values of the experimental curves and the values are also included in Table 8. Fig. 12(a) shows the plotting of the calculated and experimental $Ms._T$ values for the LTT series. There is reasonable fitting or trend between the models and the experimental data. The highest difference observed is 47 °C from van Bohemen and Wang models (Van Bohemen, 2012; Wang et al., 2000). Therefore, the $Ms._T$ estimation using the R-type thermocouple was considered adequate for this study.

Also, Schaeffler diagram was used to predict the phase(s) that might be present in the resulting WM microstructure. To do this, the calculated Cr-equivalent (Cr_eq) and Ni-equivalent (Ni_eq) in Table 6 were plotted

Table 8
Comparison of experimental and calculated $Ms._T$ values for the weld metal compositions.

LTT alloy	LTT1	LTT2	LTT3
Experimental $Ms._T$			
PS	385	351	231
PS UL	392	353	238
PS LL	378	349	224
Model predicted $Ms._T$			
Steven & Haynes	362	332	234
Andrews (linear)	369	342	260
Kung & Rayment (mod.)	364	337	257
Wang (linear)	355	339	254
van bohemian	380	354	278

UL – upper limit, LL – lower limit, PS – present study

as shown in Fig. 12(b). The diagram predicted that the resulting microstructures of the LTT series would be entirely α'. It also predicted that the microstructure of the ER70 should compose of α matrix with some α' (or other displacive transformations such as acicular ferrite can occur depending on the residual stress level and cooling conditions).

Hardness measurement

The hardness plots for the ER70 WMs and that of the LTT series are shown in Fig. 13. The highlighted number above the bar is the average hardness value of the 5 points on each WM (See Fig. 4(c)). Table 9 gives a summary of the experimental $Ms._T$, the range, and the average hardness values for the LTT series and ER70.

The hardness increased rapidly from ER70 average value of 161 to 397 and appears to remain within a narrow range for the LTT series. Hardness value up to 407 Hv was recorded for the LTT WM. The high hardness value shows that the entire microstructure is martensitic.

Macro- and microstructures of ER70 and LTT series weld metals

Typical macro- and microstructure of the ER70 WM in a 6-pass weld on X100 baseplate is shown in Fig. 14. Fig. 14(b–d) are representations of the areas b, c and d noted in Fig. 14(a) respectively. The ER70 typically contains ferrite, α (light etching), Widmanstätten ferrite, α_w (the comb like structure) and acicular ferrite, α_a (the needle like structure) as noted in Fig. 14(b). All the phases are contained in the prior austenite (γ) columnar grains. Fig. 14(c) is the overlapped region that contains α and degenerated pearlite or carbide (θ) phases. Fig. 14(d) shows microstructure having fine-grained-equiaxed α and θ/carbide dispersion. Thus, the ER70 WM produced a microstructure consisting of mixed phases of α, α_w, α_a and α_b in some few areas that are not shown here.

Table 9
Summary of $Ms._T$ and hardness values of ER70 and LTT series weld metals.

Weld metal	$Ms._T$ (exp) °C	Hardness Range (Hv)	Average Hardness (Hv)
LTT1	388 ± 7	383 - 414	397
LTT2	340 ± 3	390 - 429	407
LTT3	231 ± 7	393 - 409	401
ER70	636 ± 2	146 - 172	161

Typical macrostructures of the LTT WMs in a 6-pass weld on X100 baseplate are shown in Fig. 15 (a & b). Only LTT1 and LTT2 are presented. LTT3 has similar macrostructure. The microstructural examination was carried out on the marked areas: the bottom (1), middle (2) and top (3) as shown schematically in Fig. 15(c). The microstructures of the three zones are shown in Fig. 16 along with their $Ms._T$. There is a dramatic change in the microstructure from that of the ER70 to LTT2 composition. The increase in the alloying elements affected the phase formation and morphology. The LTT1 appears as an intermediate microstructure between the ER70 and the LTT2. The LTT1 is similar to ER70 except that what formed inside the prior γ columnar grain is fine plates of needle α' instead of α_w, α_a and α_b found in the ER70. The microstructure of the LTT at area 1 (close to the substrate), and area 3 (edge of WM) that experienced rapid cooling is equiaxed. The inner zone where the cooling is slower is columnar. Generally, the LTT microstructure is composed of α' and γ_r. The LTT3 was selected for fatigue crack growth resistant test because it has the lowest $Ms._T$, hence is expected to exert the most CRS. Also, from the cracking assessment the LTT3 did not show any crack at the weld notch.

Fatigue crack propagation study

Baseplates

Table 10 presents the number of cycles to initiate the fatigue crack (N_i), and the total number of cycles it took to stoppage (N_f) for the baseplates – S355 and X100. The stoppage time is usually when the growing crack becomes unstable and about to fail completely. The samples were not allowed to fail completely so that the crack path could be studied. The test was conducted twice, labelled – (a) and (b). In Table 10 for example, it took about 11,000 to initiate the fatigue crack from the machined notch in X100 and a crack length of 15.78 mm from the machined notch was measured after 165,000 cycles, etc. Table 10 shows that it took more cycles to initiate and grow the fatigue crack in X100 than in S355. Note that the notch tip condition is similar for all the samples. Fig. 17(a) is the plot of the a vs. N for the baseplates. The two S355 curves coincided, while there is some variation for the X100 steel. Such variation may be due to inhomogeneity inherent in thick steel materials. Fig. 17(b) shows the plot of the FCG rates. There is some

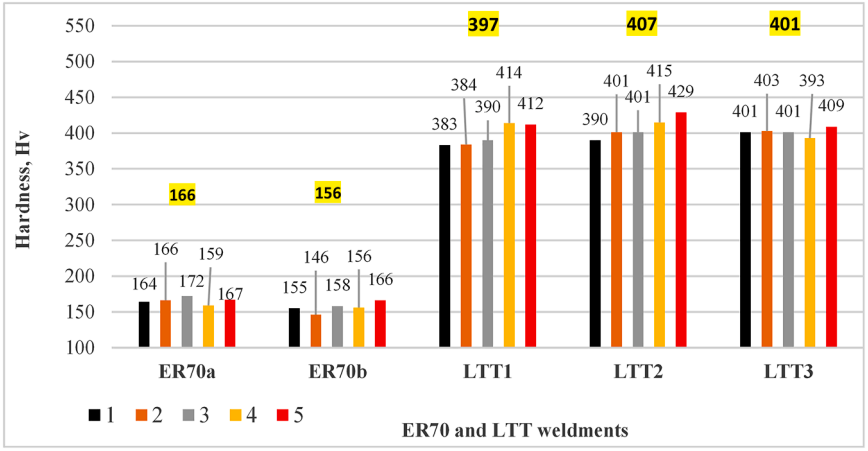

Fig. 13. Hardness plot of ER70 and LTT series weld metals.

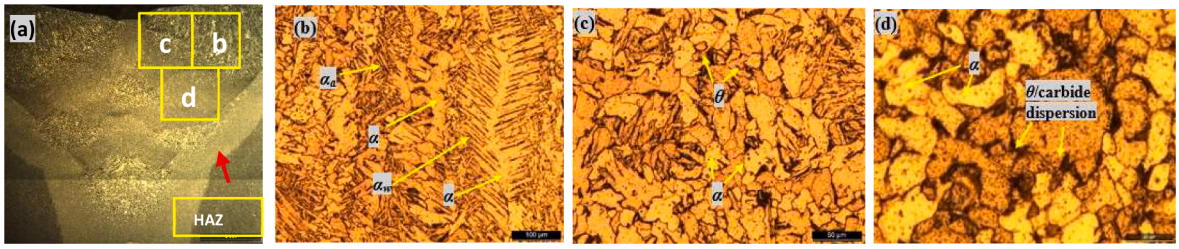

Fig. 14. Phases in the ER70S-6 weld metal microstructure.

Fig. 15. (a & b) The macrostructures of LTT1 and LTT2 weld metals, (c) the schematic of the areas of microstructural examination.

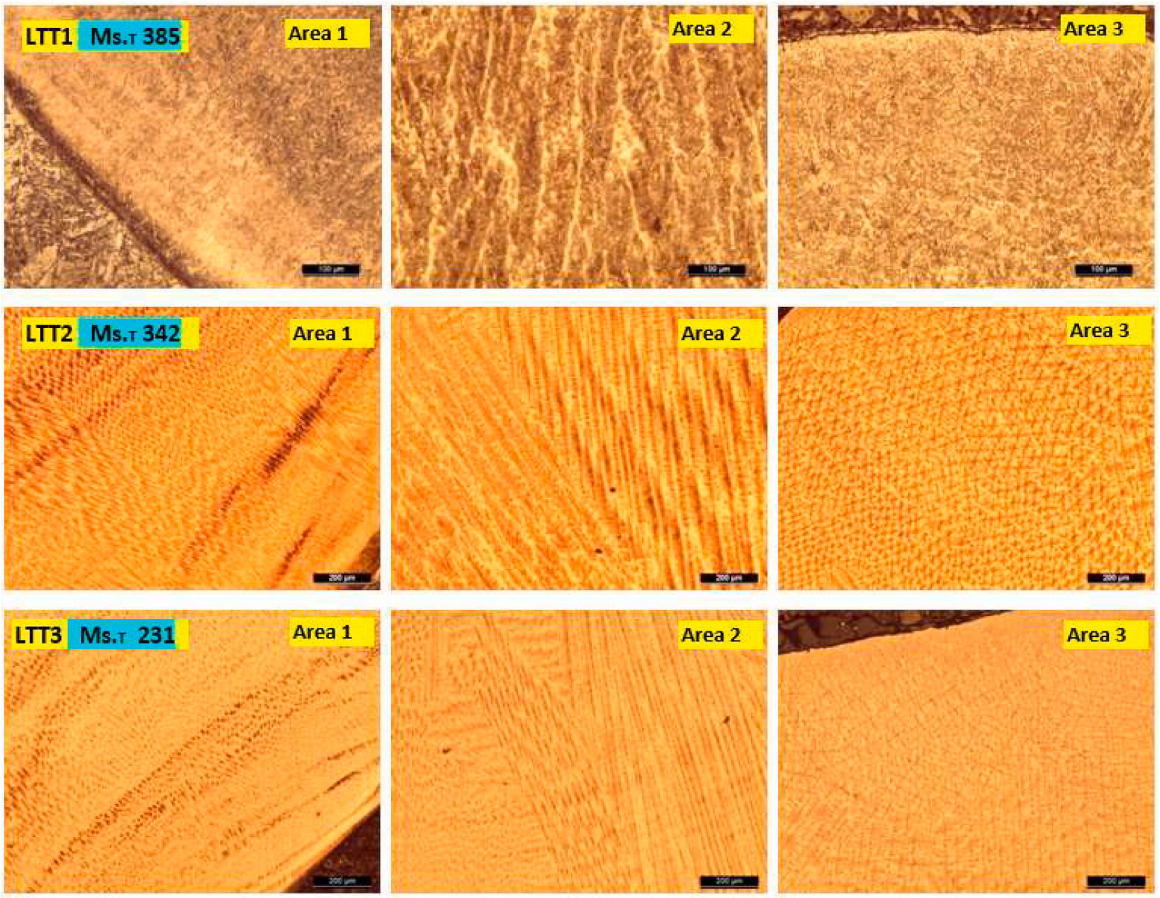

Fig. 16. Typical microstructures of the LTT weld metals.

variability in the FCG rates of the X100, but that of S355 is basically the same. Despite its reduced ductility, the FCG rate of the X100 is lower than that of the S355. That is, X100 plate has higher FCG resistance than S355. This tends to suggest that strength has more influence on the FCG resistance than ductility for ferritic steels (see Fig. 6 or Table 4). However, in steel, strength is increased by grain refinement and solid solutioning. The microstructure of the X100 consists of carbides/granular bainites distributed in the fine-grained ferrite matrix. This appears to have contributed to the crack growth resistance as compared with that of S355.

The optical fiber illumination of the crack paths in the baseplates are shown in Fig. 18. Fig. 18 (a & b) are the two tests performed for the S355

Table 10
Number of fatigue cycles to initiate and propagate the crack to stoppage or failure in the baseplates.

Baseplates	N_i	N_f	a_f
X100a	11,000	165,000	15.78
X100b	14,490	188,600	15.70
S355a	2750	115,000	16.61
S355b	3500	117,000	19.28

N_i – approximated number of cycles to initiate the crack growth at the machined notch.
N_f – approximated number of cycles to stoppage (a_f).
a_f – crack length from machined notch at stoppage.
a_0 – machined notch length = 22.5 mm.

while Fig. 18 (c & d) for the X100 samples. The crack growth was observed to be normal, continuous, and propagating fairly horizontal. Where there was deviation, it was not more than 1.5 mm from the horizontal plane. Hence, it produced a data that gave smooth quadratic curve on the *a* vs. N plot as shown in Fig. 17(a). The propagation pattern and the smooth quadratic curve are important in comparing the data obtained in this study.

ER70S-6 weldment

The baseplates were gouged and repaired with ER70 as shown in Fig. 7(–i). The notch condition was similar for all the samples tested. FCG test was carried out on ER70W(355), ER70W(100), ER70T(355) and ER70T(100). The preheating, T_i conditions and sample nomenclatures are shown in Table 11. During the fatigue test, it was observed that the position of the notch tip can affect the crack path. Fig. 19(a) shows the positioning of the notch tip outside the WM. In this case, the advancing crack front was found to consistently divert towards the HAZ. Thus, the HAZ appeared as the least resistant path for the approaching crack front. Hence, to test the WM the crack or notch tip was positioned inside it as shown in Fig. 19(b). The length of the machined notch on the C(T) is 22.5 mm. Table 11 shows the results of the FCG tests.

For the ER70W(355), the fatigue crack initiated from the notch after about 17,500 cycles. It took over 1.3 million continous cycles to propagate the crack to 2.63 mm into the WM. After the 1.3 million cycles - lasting for over 3 days, the test was terminated due to time constraints. For the ER70W(100), two tests were performed and T_i of about 150° was maintained. For ER70W(100)a, the fatigue crack initiated from the notch after about 175,300 cycles and 1.3 million cycles was recorded at a crack length of about 2.29 mm before termination of the test. For ER70W(100)b, the fatigue crack initiated after about 183,000 cycles and 1.3 million cycles was recorded at a crack length of about 9.37 mm before termination of the test. Thus, there are some microstructural variabilities in the X100 baseplate. However, 1.3 million cycles were exceeded at a subcritical crack length.

For ER70T(355), the crack started propagating from the machined notch after about 275,000 cycles. Over 1.3 million cycles were recorded at a crack length of 1.13 mm before termination of the test. For ER70T (100), the crack initiated after 155,700 cycles and 1.3 million cycles was exceeded at about 3.05 crack length. Another ER70T(100) sample was preheated using a gas flame to about 270 °C after which an T_i of about 240 °C was maintained and labelled ER70T(100)PH. Thus, the cooling rate was slower for ER70T(100)PH. The crack initiated from the machined notch after about 4500 cycles and propagated through the ER70 WM to failure after 151,500. This result tends to suggest that higher T_i and slow cooling of repaired weldment can be detrimental to its FCG resistance. The FCG test for the HAZ produced by the ER70 WM on the X100 baseplate was done twice labelled – ER70H(100)a and ER70H(100)b. Note that the tip of the notch was positioned as shown in

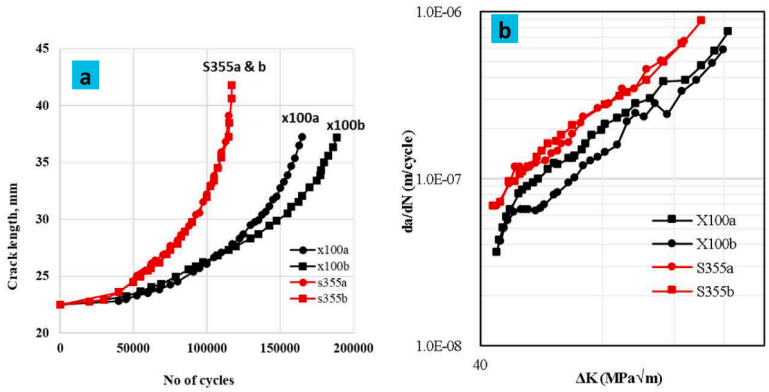

Fig. 17. FCG rates: (a) of the baseplates, S355 and X100, (b) of the ER70 weldment on X100 baseplate.

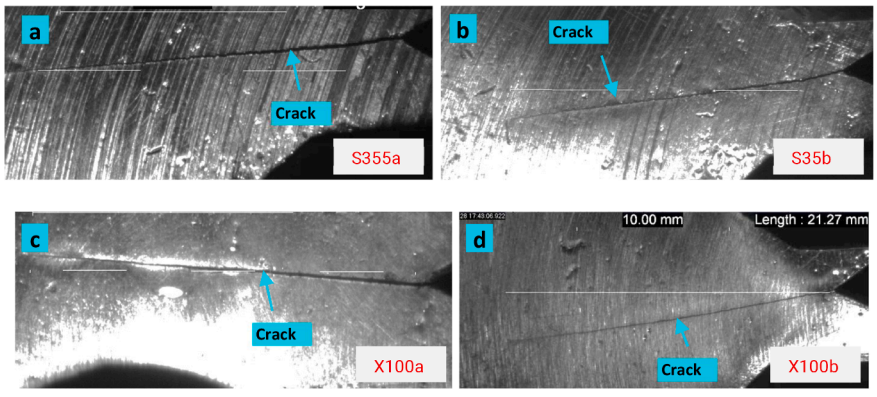

Fig. 18. Optical fiber illumination of the crack paths in the experimental baseplates.

Table 11
Sample notation and number of fatigue cycles through ER70 weld metal.

ER70	~ Ti °C	N_i	N_f	a_f
ER70W(355)	100	17,500	1,300,000	2.63
ER70W(100)a	150	175,300	1,300,000	2.29
ER70W(100)b	150	183,000	1,300,000	9.37
ER70T(355)	100	275,000	1,300,000	1.13
ER70T(100)	150	155,700	1,300,000	3.05
ER70T(100)PH	240	4500	151,500	19.25
ER70H(100)a	150	9000	138,500	18.69
ER70H(100)b	150	7000	123,190	18.06

Nomenclature: a_0 – machined notch of length 22.5 mm; WM – weld metal; T – transverse welding;.
Ti – interpass temperature; PH – whole sample pre-heated.
N_i – approximated number of cycles to initiate the crack growth at the machined notch.
N_f – number of cycles to stoppage (a_f) or failure.
a_f – crack length from machined notch at stoppage/failure.
ER70W(355) - ER70 weld metal on S355 baseplate.
ER70W(100) - ER70 weld metal on X100 baseplate.
ER70T(355) - ER70 weld metal in perpendicular direction to the crack growth front on S355 baseplate.
ER70T(100) - ER70 weld metal in perpendicular direction to the crack growth front on X100 baseplate.
ER70H(100) – Heat affected zone produced by ER70 weld metal on X100 baseplate.
ER70H(355) – Heat affected zone produced by ER70 weld metal on S355 baseplate.

Fig. 9(b). The ER70H(100) shows poor resistance in comparison with the ER70 WM.

The general observation for the ER70 weldment is that: (1) fatigue crack did not propagate through the as-welded ER70 WM within the time constraint of the experiment under relatively fast cooling. While ER70 WM is very tough, its HAZ is relatively poor in resistant the FCG. (2) The relatively rapidly cooled ER70T(355) offered the best resistance to FCG. (3) For the WM, the number of cycles needed to initiate the FCG is relatively very low in S355 in comparison with X100, even though they both exceeded 1.3 million cycles. However, the case is different for the perpendicularly aligned WM. Here, the number of cycles to initiate the fatigue crack from the machined notch in the baseplate is higher in the S355. Note that FCG resistance is higher in the X100 (see Fig. 17). This tends to show that a CRS is induced at the notch tip by the perpendicularly aligned ER70 WM and this resulted to increased number of cycles to initiate and propagate the fatigue crack through both the S355 and X100 parent metals.

The *a* vs. N for the ER70T(100)PH, ER70H(100)b and X100 are plotted in Fig. 20(a). Included in the plot is the curve S355a. The rate at which the crack propagated in the samples are plotted in Fig. 20(b). In Fig. 20(a) or (b), S355a and ER70H(100)b have almost similar FCGRs. This shows that X100 is superior to S355J2+*N* steel in terms of resistance to FCG. In Fig. 20(b), the FCG rate of ER70T(100)PH is lower or within the same range of the X100 baseplate, though propagating faster at higher stress intensity factor range (ΔK). This tends to suggest that aligning the WM in a perpendicular direction to the crack front can produce a FCG resistance similar to that of the baseplate. Here, the weak HAZ is placed in a less favourable position for the crack to grow into than when the HAZ is in parallel with the direction of the crack growth front.

Fig. 20(c) is the crack path across the ER70T(100)PH. Note the C(T) surface was polished with 400 grit abrasive paper, producing undistinguishable smooth surface - which indicates the soundness of the welding process. For the ER70T(100)PH, initially, the crack was propagating in the X100 baseplate up to position 1, after which it diverted through path 2 into the perpendicularly aligned WM. The effect of this diversion is a corresponding strong retardation of the FCG rate as shown by the encircled region in Fig. 20(b). Fig. 20(d) is the typical crack path across the ER70H(100) and there is relatively no crack diversion.

If we assumed that the crack growth steady region is in the range $\Delta K = 75 - 150\ \text{MPa}\sqrt{\text{m}}$, then the mean Paris curves for Fig. 20(b) are shown in Fig. 20(e) and the Paris law constants given in Table 12. Curves with higher *m* value are more tilted. Hence, at a lower ΔK, say, 75 $\text{MPa}\sqrt{\text{m}}$, ER70T(100)PH had the lowest FCGR, but the propagation rate increased more rapidly with increase in the ΔK value. At about $\Delta K = 110\ \text{MPa}\sqrt{\text{m}}$, the FCGR of the ER70T(100)PH became higher than that of X100 baseplate. The FCGRs of the HAZ(100) and S355 samples remained higher both at low and high ΔK values. Fig. 20(e) shows clearly that X100 baseplate. including its HAZ has better fatigue resistance than S355J2+N steel.

LTT alloy weldment

Similarly, the C(T) specimens extracted from the baseplates were gouged and repaired with LTT3 as shown in Fig. 7 (g, h & i). The excess WM resulting from the weld deposition on the C(T) sample was ground off, as shown in Fig. 7 (j, k & l), before FCG testing. Repairs on S355 or X100 baseplates are indicated in brackets. The sample nomenclatures are defined in Table 13. Many a time, microstructural examination is often done after the experiment has been concluded. In this case, the series of events that occurred as the crack is growing are not often captured. The optical fiber illumination used in this study helped to virtualize in-situ how the crack is propagating during the experiment. This is found to be extremely useful in observing crack growth behaviour in the martensitic alloys.

Fig. 21 shows the illumination of the crack path in the LTT3 samples. Inconsistency was observed in the way crack propagated in the LTT alloy which was different to that observed in the ER70. Fig. 21(a and b) are generally the crack behaviour in the LTT3W(100). Arrow 1 shows the main crack growth from the machined notch and arrow 2 shows crack initiating from somewhere else in the WM and propagating in the same direction as the main crack. For LTT3W(355), only one prominent crack front was observed as shown in Fig. 21(c), but there were small cracks that initiated away from the main crack. Fig. 21(d, e, and f) show the observation of the crack growth from initiation to a length up to 15 mm from the machined notch in LTT3H-W(100). The crack tip was positioned so that the crack propagates through the HAZ. It was assumed that if the HAZ or fusion line is the weakest, then the fatigue crack would prefer to grow through it than elsewhere. In Fig. 21(d) arrow 1 shows the main crack growth direction and arrow 2 shows crack initiating from somewhere else in the WM and propagating parallel and ahead of the

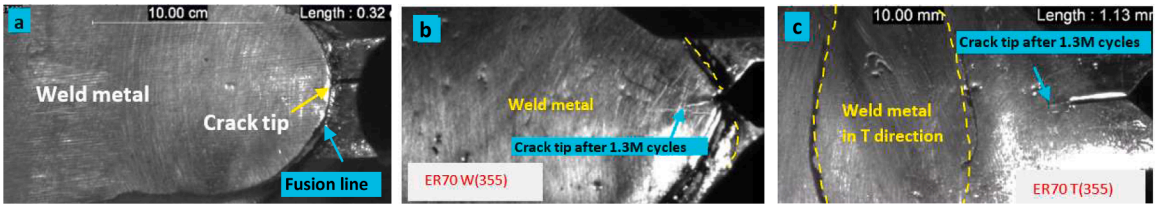

Fig. 19. Crack tip positioning during ER70 testing; (a) crack tip outside the weld metal, (b) crack tip inside the weld metal, (c) weld metal in perpendicular direction to the FCG front.

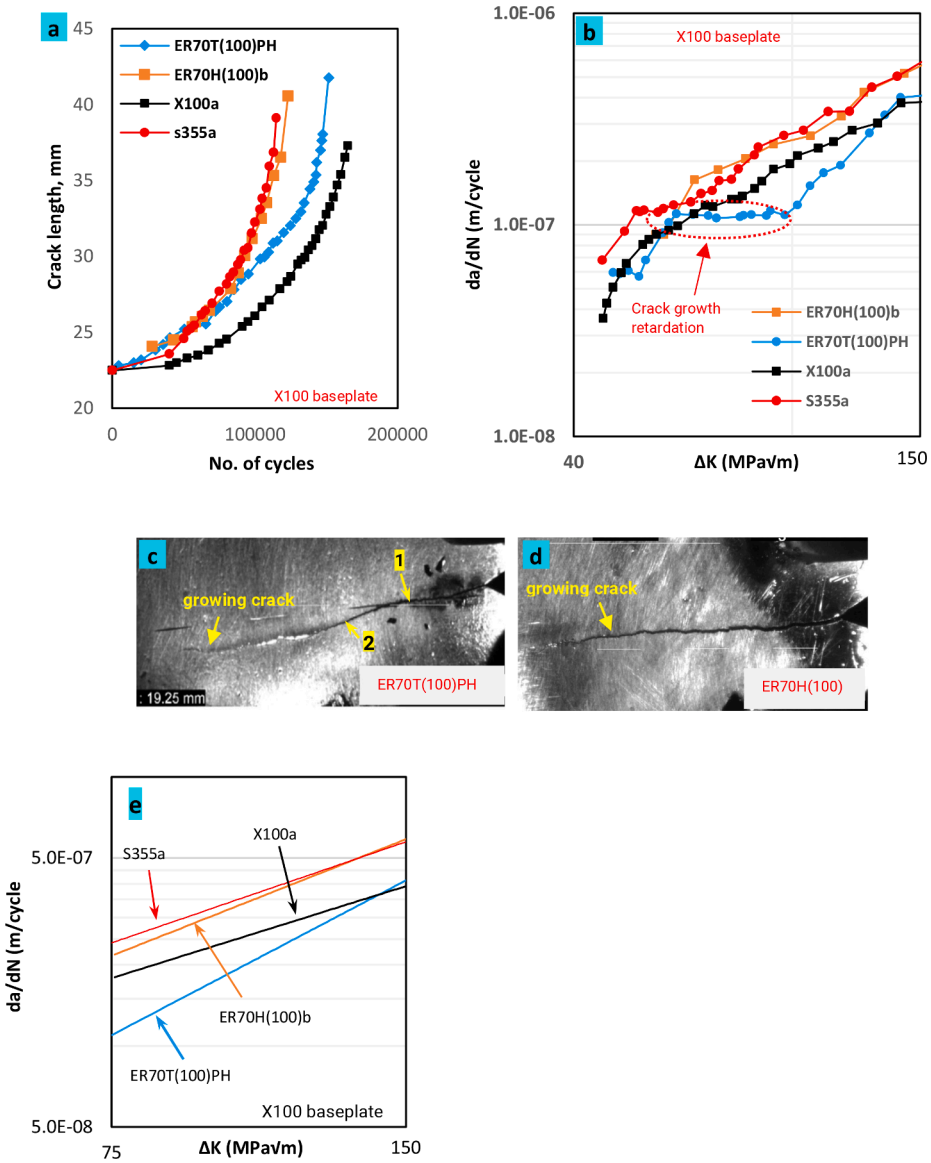

Fig. 20. FCGR test for ER70 weldment on the X100 baseplate: (a) *a* vs. N for the transverse weld, HAZ and baseplates, (b) comparison of the FCG rates, (c & d) illuminated crack path in the ER70T(100) and ER70H(100) test samples, (e) mean Paris curves for the data in (b).

Table 12
The Paris laws for the X100, ER70H and ER70T(PH).

Specimen	FCGR(da/dN)
ER70H(100)b	$2.0 \times 10^{-11} \Delta K^{2.12}$
ER70T(100)PH	$6.0 \times 10^{-13} \Delta K^{2.82}$
X100a	$1.0 \times 10^{-10} \Delta K^{1.68}$
S355a	$9.0 \times 10^{-11} \Delta K^{1.84}$

main crack front. Fig. 21(e) shows that as the crack 2 grew ahead of crack 1, the crack 1 eventually joined the crack 2. Note that this would have been interpreted as a normal diversion by the main crack if Fig. 21 (d) stage event was not observed. As the crack 2 continued to grow, another crack 3 initiated and grew ahead of it as shown in Fig. 21(f). As the crack 3 grew, crack 2 eventually joined it to form a single front.

In Fig. 21(g), the arrow 1 shows a crack that initiated and propagated towards the HAZ in LTT3H-W(355). After growing to about 5.0 mm from the notch tip, another crack 2 initiated and grew in the WM ahead of it. The growth of the new crack 2 slowed down temporarily the growth of

Table 13
LTT3 Test Samples nomenclature.

Nomenclature:
LTT3W – LTT3 weld metal
LTT3W(100) – LTT3 weld metal on X100 baseplate
LTT3W(355) - LTT3 weld metal on S355 baseplate
LTT3T(100) - LTT3 weld metal in perpendicular direction to the crack growth front on X100 baseplate
LTT3H(100) - HAZ produced by LTT3 WM on X100 baseplate
LTT3H-W(355) - Crack tip position to pass through HAZ, but diverted into the weld metal on S355 baseplate
LTT3H-W(100) - Crack tip position to pass through HAZ, but diverted into the weld metal on X100 baseplate

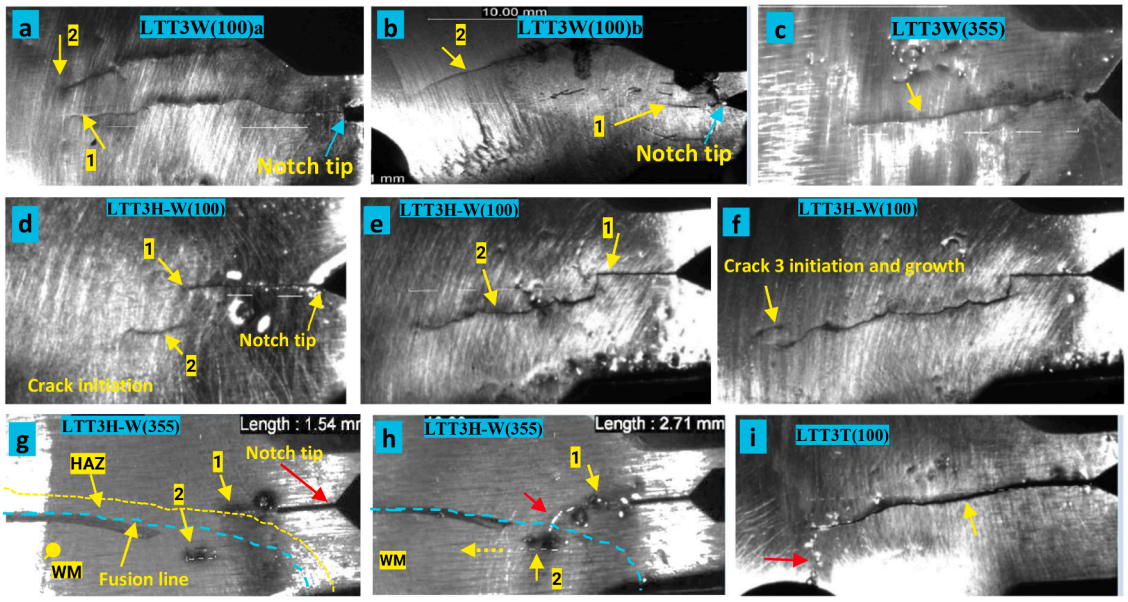

Fig. 21. Optical fiber illumination of the crack path in the LTT alloy.

crack 1. At the point of measurement, the crack 2 had grown to a length of about 1.54 mm. After the crack 2 had grown to a length of about 2.71 mm, the crack 1 diverted and joined with crack 2 and the new crack front grew in the direction indicated by the broken yellow arrow in Fig. 21(h). After the tests, it was observed that all the LTT samples with the crack tips intended to propagate through the HAZ diverted into the WM. This diversion was facilitated by crack forming in the WM ahead of the main crack. This implies that the LTT WM itself has poor resistance to FCG, but its HAZ appears to have better fatigue resistance. Fig. 21(i) is the FCG in the LTT3T(100). Initially, the crack grew normally from the baseplate into the perpendicularly aligned WM. However, when the crack tip encountered what appears as a 'fault line' in the WM, it was diverted along the direction of the 'fault line' (as shown by the red arrow) and continued to grow in that direction to failure. It is therefore believed that the martensitic WM has 'fault lines' that served as sites for crack formation and this reduces its resistance to FCG. The LTT3 cracking behaviour was not observed in the baseplates (Fig. 18) and ER70 (Fig. 20) tests. In this instance, we can exert that the microstructure of the WM influenced the mode of fatigue crack propagation behaviour.

In general, the mode of crack propagation in the LTT alloy is completely different from that of wrought steel or HAZ in the base metal. It was observed that when the crack initiated elsewhere in the LTT3 the growth rate of the main crack was drastically reduced or halted. Several fatigue cycles were then needed for the cracks to continue to grow in parallel or to join the second crack to form a single crack front. The initiation of crack elsewhere in the WM as the main crack propagated resulted in uneven variation of a vs. N values across the WM. This is the reason why number of cycles to initiation and failure were used to describe the LTT3 fatigue performance. During the test, the fatigue machine was set in a position such that if the C(T) crack mouth opening exceeds 0.6 mm the test is terminated, and failure is considered to have occurred. Table 14 presents the crack initiation cycles, the length of the crack and number of cycles before the 0.6 mm crack mouth opening distance was exceeded.

The fatigue crack test through the WM (LTT3W(100)) was performed four times – labelled, a, b, c, and d, in a bid to confirm the results obtained. For the perpendicularly aligned WM sample (LTT3T(100)), the test was performed three times – labelled a, b, and c. All the tests where the C(T) notch tip is positioned inside the LTT3 WM are coloured orange in Table 14. Table 14 shows that the LTT3 WM had poor resistance to

Table 14
Number of fatigue cycles to crack mouth opening of 0.6 mm.

LTT3	~ Ti °C	N_i	N_f	a_f
LTT3W(100)a	150	2937	98,000	18.13
LTT3W(100)b	150	3100	112,500	17.91
LTT3W(100)c	240	8705	93,595	10.72
LTT3W(100)d	240	5848	92,326	12.92
LTT3W(355)	100	2100	152,500	17.30
LTT3H-W(100)	150	2780	119,075	17.08
LTT3H-W(355)	150	2500	92,500	17.15
LTT3T(100)a	150	10,100	155,000	17.46
LTT3T(100)b	240	8534	198,047	17.20
LTT3T(100)c	240	9291	160,937	16.58
LTT3H(100)	150	7399	281,106	16.07
X100a	–	11,000	165,000	15.78
X100b	–	14,490	188,600	15.70
S355a	–	3500	117,000	19.28

a_f – crack length from machined notch at stoppage/failure.
N_i – approximated number of cycles to initiate the crack growth at the machined notch.
N_f – number of cycles to stoppage (a_f) or failure.
Ti – interpass temperature.

FCG in comparison with ER70 WM (see Table 11) - considering the number of cycles to stoppage/failure. Table 14 also shows that the number of cycles to initiate FCG in the LTT3 WM is very low compared with that of ER70 (see Table 11). As already mentioned, LTT3H-W is the specimen where the notch tip was positioned to pass through HAZ but diverted into the WM (see Fig. 21 (d–h)). The LTT3H-W is coloured gold in Table 14 and it showed poor resistance to FCG. The transversely aligned WM, LTT3T is coloured grey, and it appears to have performed better than the LTT3W (orange colour). However, it must be noted that the fatigue crack in LTT3T propagated from the baseplate into the WM while in the LTT3W the fatigue crack propagated entirely through the WM. The diversion of the crack into the WM in LTT3H-W samples tends to confirm the poor FCG resistance of the LTT3 WM.

In sample LTT3H(100), coloured green in Table 14, the crack successfully passed through the HAZ. The LTT3H(100) offered better FCG resistance than the LTT3W(100). Table 14 also shows that the LTT3H (100)) had the highest resistance to FCG and performed better than the X100 baseplate. This suggests that the LTT3 WM induced a compressive stress in the X100 HAZ which increased its FCG resistance more than the

parent metal. Note that in Table 14, the LTT3H-W(100) and LTT3T(100) performed better than the S355 baseplate. Also, ER70H(100) resisted FCG equally or better than the S355 baseplate. In other words, X100 baseplate generally resisted the FCG better than S355J2+*N* steel. This implies that for fatigue resistant applications, X100 is superior to S355J2+*N* steel.

Table 15 shows the comparison of the FCG data of the LTT3 weldments with ER70 on X100 baseplate. For clarity and to be conservative - where the experiment is repeated, the data selected (from Table 14) are for samples with lowest number of cycles and higher crack length to failure. Fig. 22 shows the plotting of the FCG data of the samples in Table 15. For the LTT alloy, the *a* vs. N plot did not produce a true parabolic curve as in Fig. 20(a). This is due to cracks nucleating at more than one place during propagation test. In fact, the mode of crack propagation in the LTT alloy did not satisfy ASTM E647–15 (ASTM, 2015) requirement for determination of valid ΔK using the equation in Section 3.4. This makes it difficult to generate comparative FCGR curves.

Table 15 or Fig. 22 simply shows that the LTT3H(100)) has the highest resistance to FCG, while LTT3 WM has least resistance. The transversely aligned WM, LTT3T(100) and ER70T(100)PH performed better than the ER70H(100) and LTT3H-W(100). Another important observation here is that the *a* vs. N curves of ER70H(100) and LTT3H-W (100) are similar. For the LTT3H-W(100), the FCG resistance is higher than that of ER70H(100) at the early stage of crack growth – which is when the crack was propagating through the HAZ. Upon diversion into the LTT3 WM, the crack growth rate became similar to that of ER70H (100). This tends to show that the microstructure of the HAZ produced by the ER70 WM is similar to that of the LTT3 WM. Since the HAZ on X100 is likely to contain martensite and/or other displacive transformation phases, it shows that martensite has poor resistance to FCG, and presence of CRS appears to be the explanation why LTT3H(100) has the highest FCG resistance in Table 15.

Summary of the FCG results

In summary, ER70T(355) showed the highest resistance to fatigue crack initiation and propagation. Since S355 had lower fatigue resistance than X100 (see Table 10 or Fig. 17), the result then suggests that the perpendicularly aligned ER70 WM induced a CRS at the machined notch tip which resulted to the high fatigue resistance. The CRS also appears to be the reason why ER70T(100) exceeded the 1.3 million cycles mark. ER70 WM was observed to be very tough as the fatigue crack found it extremely difficult to propagate through the WM. As expected, the HAZ produced by the ER70 WM on X100 plate had lower fatigue resistance than the X100 baseplate and more than 10 times lower than that of ER70 WM. It was generally observed that when fatigue crack grew towards an area repaired with ER70, it was always diverted towards its HAZ. Thus, the HAZ of ER70 weldment is weak in resisting crack propagation and this concealed the benefit of the tough ER70 WM. The fatigue resistance of the weldment could be improved by placing the WM perpendicularly to the direction of the crack front. In this way, the weak HAZ is placed in a less favourable position for the FCG than when the HAZ is in parallel with the direction of the crack growth front. Excessive preheating or slow cooling of weldment was observed to reduce drastically the FCG resistance.

Table 15
Comparison of LTT3 with ER70 on X100 baseplates.

LTT3	~ Ti °C	N_i	N_f	a_f
X100a	–	11,000	165,000	15.78
ER70H(100)b	150	7000	123,190	18.06
ER70T(100)PH	240	4500	151,500	19.25
LTT3W(100)a	150	2937	98,000	18.13
LTT3H-W(100)	150	2780	119,075	17.08
LTT3H(100)	150	7399	281,106	16.07
LTT3T(100)a	150	10,100	155,000	17.46

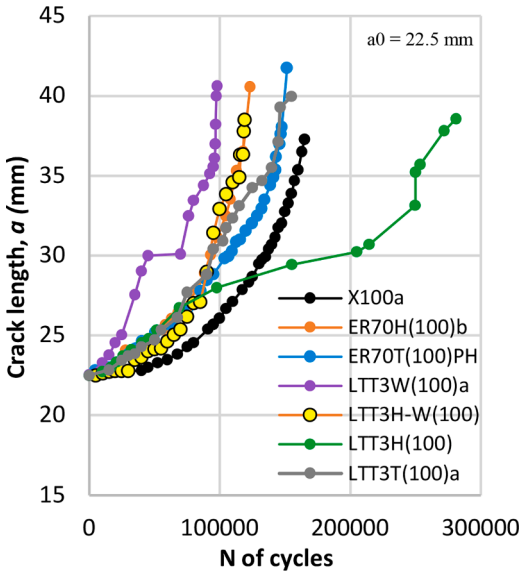

Fig. 22. The *a* vs. N for the LTT alloy.

The LTT3 WM had the lowest FCG resistance. The ER70 WM was more than 10 times better in resisting the fatigue crack growth than LTT3 WM. An improvement was observed when the LTT3 WM was aligned perpendicularly, but this increase is more than 10 times less than that of ER70T. LTT3H(100) performed better than ER70H(100) by an approximate factor of 2. Though the ER70 WM resisted the crack propagation more than 10 times that of LTT3 WM, the HAZ produced by the LTT3 resisted crack growth more than that of the ER70. This is due to the CRS induced around the LTT3 weldment. Despite its low Ms_T and the anticipated beneficial effect of the induced CRS, LTT3 WM had the lowest FCG resistance. It is therefore believed that the LTT3 WM had inherent microstructural feature that reduced its resistance to FCG. The reasons why the LTT3 WM performance was below expectations and the method to improve its FCG resistance would be examined in the subsequent study. Also, to be investigated is the mechanism of FCG in ferritic and martensitic steels. Further studies and residual stress measurements are ongoing to enable comprehensive characterisation of the LTT alloy behaviour.

Conclusions

1. API 5 L X100 baseplate resisted FCG more than the S355J2+*N* baseplate. That is, for fatigue resistant applications, X100 is superior to S355J2+*N* steel.
2. Weld metal interpass temperature and its orientation relative to the crack front are important factors in FCG resistance of welded joints.
3. S355J2+*N* and API 5 L X100 baseplates repaired with ER70S-6 having the WM aligned perpendicular to the crack front showed the highest resistance to fatigue crack initiation and propagation. It is believed that the ER70S-6 WM induced a CRS at the notch tip which resulted to the high fatigue resistance.
4. ER70S-6 WM obtained under relatively fast cooling is observed to be very tough because fatigue crack found it extremely difficult to propagate through it. While the WM is exceptionally tough the associated HAZ has poor resistance to crack growth which obscured the benefit of the tough WM. High heat input or condition that results to slow cooling of ER70S-6 weldment deteriorates its resistance to FCG.
5. Unfortunately, despite its low Ms_T of 231 ± 7 and the anticipated beneficial effect of induced CRS, the LTT alloy studied had the lowest FCG resistance. An improvement is obtained when the WM is aligned

perpendicularly to the crack front, but this increase is more than 10 times less than that of ER70S-6. It is believed that the LTT alloy has intrinsic microstructural feature or a 'fault line' that reduced its resistance to FCG irrespective of the amount of CRS in the WM. While the LTT alloy WM has poor resistance to FCG, the associated HAZ resisted FCG more than the HAZ associated with ER70S-6 WM.

CRediT authorship contribution statement

Victor Igwemezie: Conceptualization, Data curation, Formal analysis, Funding acquisition, Investigation, Methodology, Writing – original draft. **Ali Mehmanparast:** Supervision, Writing – review & editing. **Supriyo Ganguly:** Supervision, Writing – review & editing, Conceptualization, Project administration.

Declaration of competing interest

The authors declare that they have no known competing financial interests or personal relationships that could have appeared to influence the work reported in this paper.

Data availability

Data will be made available on request.

Acknowledgements

This project is funded through EPSRC Doctoral prize. I would like to thank the following for their wonderful support: John Thrower, Flemming Nielsen and Nisar Shah for the lab equipment set up and troubleshooting, Dr Chenglei Alex Diao for support in robot programming, Steve Pope and Tracey Roberts for the optical microscopy.

References

Masubuchi K. Analysis and Control of Residual Stresses, Distortion and Their Consequences in Welded Structures. vol. 33. Oxford; New York: Pergamon Press; 1980.

Withers, P.J., Bhadeshia, H.K.D.H., 2001. Residual stress part 2 - Nature and origins. Mater Sci Technol 17, 366–375. https://doi.org/10.1179/026708301101510087.

Fricke, W., 2005. Effects of residual stresses on the fatigue behaviour of welded steel structures. Mater Sci Eng Technol 36, 642–649. https://doi.org/10.1002/MAWE.200500933.

Ainsworth, R.A., Sharples, J.K., Smith, S.D., 2000. Effects of residual stresses on fracture behaviour - experimental results and assessment methods. J. Strain. Anal. Eng. Des. 35, 307–316. https://doi.org/10.1243/0309324001514431.

Moyer, J.M., Ansell, G.S., 1975. The Volume Expansion Accompanying the Martensite Transformation in Iron-Carbon Alloys. Metall Trans A 6A, 1785–1791.

Francis, J.A., Bhadeshia, H.K.D.H., Withers, P.J., 2007. Welding residual stresses in ferritic power plant steels. Mater Sci Technol 23, 1009–1020. https://doi.org/10.1179/174328407X213116.

Bhadeshia, H.K.D.H., Francis, J.A., Stone, H.J., Kundu, S., Rogge, R.B., Withers, P.J., et al., 2007. Transforamtion Plasticity in Steel Weld Metals. Proceeding 10th Int Aachen Weld Conf.

Ohta A., Suzuki N., Maeda Y., Hiraoka K., Nakamura T. Superior fatigue crack growth properties in newly developed weld metal. vol. 21. 1999.

Ohta, A., Watanabe, O., Matsuoka, K., Maeda, Y., Suzuki, N., Kubo, T., 1999b. Fatigue strength improvement of box welds by low transformation temperature welding wire by PWHT. Int Inst Weld. Document X.

Ota, A., Maeda, Y., Suzuki, N., Watanabe, O., Kubo, T., Katsuoka, K., 2001. Fatigue strength improvement of box welds using low transformation temperature welding material. Tripled fatigue strength by post weld heat treatment. Weld Int 19, 373–376. https://doi.org/10.1080/09507110209549487.

Ohta, A., Matsuoka, K., Nguyen, N.T., Maeda, Y., Suzuki, N., 2003. Fatigue strength improvement of lap joints of thin steel plate using low-transformation-temperature welding wire. Weld J (Miami, Fla) 82.

Ota, A., Shiga, C., Maeda, Y., Suzuki, N., Watanabe, O., Kubo, T., et al., 2000. Fatigue strength improvement of box-welded joints using low transformation temperature welding material. Weld Int 14, 801–805. https://doi.org/10.1080/09507110009549271.

Ohta, A., Suzuki, N., Maeda, Y., Hiraoka, K., Nakamura, T., 1999c. Superior fatigue crack growth properties in newly developed weld metal. Int. J. Fatigue 21, 113–118. https://doi.org/10.1016/s0142-1123(99)00062-6.

Eckerlid, J., Nilsson, T., Karlsson, L., 2003. Fatigue properties of longitudinal attachments welded using low transformation temperature filler. Sci Technol Weld Join 8, 353–359. https://doi.org/10.1179/136217103225005525.

Ooi, S.W., Garnham, J.E., Ramjaun, T.I., 2014. Review: low transformation temperature weld filler for tensile residual stress reduction. Mater. Des. 56, 773–781. https://doi.org/10.1016/j.matdes.2013.11.050.

Karlsson, L., Mraz, L., 2011. Increasing fatigue life using Low Transformation Temperature (LTT) welding consumables. Zváranie Svarováni 1–2, 8–15.

Bhatti, A.A., Barsoum, Z., Van Der Mee, V., Kromm, A., Kannengiesser, T., 2013. Fatigue strength improvement of welded structures using new low transformation temperature filler materials. Procedia Eng. 66, 192–201. https://doi.org/10.1016/j.proeng.2013.12.074.

Matsuzaki, T., Hiraoka, K., Zhongyuan, F., Ma, N., Murakawa, H., Kano, S., et al., 2020. New LTT Welding Material and All-Position Repair Welding with Elongated Bead for Super-Long Fatigue Life of Boxing Fillet Joints. J Japan Soc Nav Archit Ocean Eng 32, 153–161. https://doi.org/10.2534/jjasnaoe.32.153.

Hensel, J., Nitschke-Pagel, T., Dixneit, J., Dilger, K., 2020. Capability of martensitic low transformation temperature welding consumables for increasing the fatigue strength of high strength steel joints. Mater Test 62, 891–899. https://doi.org/10.3139/120.111562.

Miyata, M., Suzuki, R., 2015. Welding process and consumables aimed at improving fatigue strength of joints. R D Res Dev Kobe Steel Eng Reports 65, 16–20.

Miki, C., Hanji, T., Tokunaga, K., 2012. Weld repair for fatigue-cracked joints in steel bridges by applying low temperature transformation welding wire. Weld World 56, 40–50. https://doi.org/10.1007/BF03321334.

Karlsson, L., Mráz, L., Bhadeshia, H.K.D.H., Shirzadi, A.A., 2010. Comparison of alloying concepts for Low Transformation Temperature (LTT) welding consumables. Biul Inst Spaw 5, 33–39.

Igwemezie, V., Shamir, M., Mehmanparast, A., Ganguly, S., 2022. A review of LTT welding alloys for structural steels: design, application and results. J Adv Join Process 5. https://doi.org/10.1016/j.jajp.2022.100110.

Evans, G.M., 1980. Effect of Manganese on the Microstructure and Properties of All-Weld-Metal Deposits. Weld J (Miami, Fla) 59, 67s-75s.

Overview of equations for estimating Ms. Ernst Abbe Univ Jena, Univ Appl Sci 2022:1–6. https://www.eah-jena.de/fileadmin/user_upload/eah-jena.de/fachbereich/scitec/SciTec-Personen/Kunert_Maik/Predicting_the_Ms_-_Overview_of_Equations.pdf (accessed June 3, 2022).

Gramlich, A., van der Linde, C., Ackermann, M., Bleck, W., 2020. Effect of Molybdenum, aluminium and boron on the phase transformation in 4 wt.-% manganese steels. Results Mater 8.

ASTM. ASTM E647-15: Standard test method for measurement of fatigue crack growth rates. 2015. 10.1520/E0647-15.2.

BSI. BS EN ISO 11782-2:2008: Corrosion of metals and alloys — Corrosion fatigue testing —Part 2: Crack propagation testing using precracked specimens. vol. 3. 2008.

Moe, Y.A., Hasib, M.T., Paul, M.J., Amraei, M., Ahola, A., Kruzic, J., et al., 2023. Experimental study on the fatigue crack growth rates of welded ultra-high strength steel plates. Adv Struct Eng 0, 1–18. https://doi.org/10.1177/13694332231180372.

Song, W., Wang, P., Wan, D., Qian, G., Correia, J., Berto, F., 2021. Fatigue crack growth behavior of Ni-Cr-Mo-V steel welded joints considering strength mismatch effect. Int. J. Fatigue 151. https://doi.org/10.1016/j.ijfatigue.2021.106389.

Jacob, A., Mehmanparast, A., D'Urzo, R., Kelleher, J, 2019. Experimental and numerical investigation of residual stress effects on fatigue crack growth behaviour of S355 steel weldments. Int. J. Fatigue 128. https://doi.org/10.1016/j.ijfatigue.2019.105196.

Igwemezie, V., Mehmanparast, A., Kolios, A., 2018. Materials selection for XL wind turbine support structures: a corrosion-fatigue perspective. Mar Struct 61, 381–397. https://doi.org/10.1016/J.MARSTRUC.2018.06.008.

Kromm, A., 2011. Transformation Behavior and Residual Stresses When Welding New Types of LTT Filler Materials. Otto von Guericke University, Magdeburg.

Guo, L., Roelofs, H., Lembke, M.I., Bhadeshia, H.K.H.D., 2017. Modelling of recalescence effect on austenite decomposition. Mater Sci Technol 33, 1–17. https://doi.org/10.1080/02670836.2017.1282693.

Van Bohemen, S.M.C., 2012. Bainite and martensite start temperature calculated with exponential carbon dependence. Mater Sci Technol 28, 487–495. https://doi.org/10.1179/1743284711Y.0000000097.

Wang, J., Van Der Wolk, P.J., Van Der Zwaag, S., 2000. Determination of martensite start temperature in engineering steels. Part I. Empirical relations describing the effect of steel chemistry. Mater Trans JIM 41, 761–768. https://doi.org/10.2320/matertrans1989.41.761.

Steven, W., Haynes, A., 1956. The Temperature of Formation of Martensite and Bainite in Low-Alloy Steels. J Iron Steel Inst 183, 349–359. https://doi.org/10.4236/jamp.2017.58127.

Andrews, K., 1965. Empirical formulae for the calculation of some transformation temperatures. J Iron Steel Inst 203, 721–729.